ARTICLE OPEN

Check for updates

Understanding the passive behaviour of low-chromium high-strength *Hybrid* steel in corrosive environments

Cem Örnek[1,2]✉, Beste Payam[1], Andrei Gloskovskii[3], Kürşat Kazmanlı[1], Nourhan Mohamed[1], Bora Derin[1], Mustafa Ürgen[1], Chin-En Chou[4], Hung-Wei Yen[4], Burçak Avcı[1] and Steve Ooi[5,6]

We investigated the unique passive behaviour of Hybrid steel in de-aerated sulfuric acid and aqueous sodium chloride solutions through corrosion tests, surface analysis, and thermochemical modelling. Electrochemical measurements confirmed that Hybrid steel possesses stainless steel characteristics, including passivity, breakdown, and pitting, akin to low-alloyed stainless steel. Synchrotron hard X-ray photoelectron spectroscopy revealed a dynamically protective nanoscale passive film composed of Fe, Cr, Ni, and Al oxides, contributing to its stainless nature. The presence of Al and Ni enhances Cr's role in forming a spontaneously passive and protective surface, resulting in exceptional corrosion resistance in acidic and chloride-containing solutions. Hybrid steel's surface oxides remain robust even beyond the Cr(III)-to-Cr(VI) redox potential, distinguishing it from other stainless steels. This work demonstrates the potential for designing sustainable stainless steel with high-strength properties without requiring the conventional Cr threshold concentration of 10.5 per cent.

npj Materials Degradation (2023)7:71 ; https://doi.org/10.1038/s41529-023-00392-z

INTRODUCTION

Stainless steel owes its exceptional corrosion resistance to its passive film that forms spontaneously on the surface[1,2]. The native passive film of standard stainless steel is a hydrated chromium-rich oxide or oxyhydroxide in the form of $Cr_2O_3 \cdot Cr(OH)_3$ and iron oxyhydroxide species with a thickness of about 2 nm, with temperature having impact on composition and thickness[3–6]. The surface oxide has no fixed composition and structure; there is a gradual change in composition across the thickness and lateral space[5,7–10]. It has often been reported that the surface oxide of stainless steel has a bilayer structure, i.e., an inner layer rich in trivalent chromium and an outer layer rich in ferric compounds[4,5,7,10]. Other elements, such as molybdenum, silicon, and nitrogen, can also participate in oxide or hydroxide formation depending on the alloying elements and their concentration[4,8,11,12].

We have shown in earlier work using CalPhaD-based thermochemical calculations that nickel cannot form the native passive film of 25Cr-7Ni super duplex stainless steel, and the composition is a spinel-mixed type of oxide, primarily $FeCr_2O_4$[13]. These calculations agree with our synchrotron X-ray analyses[5,7,9]. However, bi- or trivalent nickel oxide/oxyhydroxide can be formed when the steel is anodically polarized. Hence, nickel is not a central contributor to the passive film of stainless steel. However, it has been demonstrated that the enrichment of nickel beneath the oxide, known as the surface alloy layer, provides a barrier to the dissolution kinetics, resulting in increased corrosion resistance[5].

Nickel behaves somewhat differently in steel alloys. It has been known that nickel enhances its mechanical properties, such as toughness and weldability, while increasing corrosion resistance in specific applications. In addition, the presence of nickel can reduce the corrosion rate of steel. In such cases, unlike in stainless steel, nickel oxide forms a significant part of the surface oxide of low-alloyed steel and can impart pseudo-passivity. Unlike stainless steel, low-alloy steels show low polarization resistance in corrosive electrolytes and undergo rapid metal dissolution. Anodic polarization of stainless steel increases the electrolyte's oxidizing power and alters the surface oxide's composition and structure[4,5,7,9,14]. As a result, stainless steel can undergo an active-to-passive transition during electrochemical polarization or oxidizing media. The surface oxide in the passive regime is then highly dense, coherent and protective[14]. However, low-alloy steels usually do not show an active-to-passive transition in chloride-bearing electrolytes.

Stainless steel requires a chromium concentration of at least 10.5 wt.-% that must be homogeneously dispersed within the iron alloy[15,16]. This threshold is due to the percolation network of chromium atoms forming a continuous bond with oxygen along the entire surface[17]. Chromium is a more active element than iron and can create highly dense and capacitive oxide. Although the dielectric constant of iron oxides is higher than that of chromium oxide, charge transport through chromium oxide is far more sluggish due to more effective compactness and lower defect density. Therefore, the corrosion resistance of stainless steel increases with the chromium concentration[15]. However, most engineering steel used in the industry is protected against corrosion by extrinsic means, such as coatings, inhibitors or cathodic protection. Due to high prices, highly-alloyed stainless steel is limitedly used. Therefore, the industry needs a range of high-strength steels that resists material degradation due to corrosion, high-temperature oxidation or tribological attack that is cheap and sustainable at the same time.

Hybrid steel is a high-strength steel that meets the requirements regarding strength, high-temperature degradation, costs and environmental sustainability. The superior strength originates from a double precipitation hardening mechanism in which carbides and aluminides strengthen the martensitic matrix[18]. The tempering (or ageing) treatment promotes the precipitation of

[1]Istanbul Technical University, Department of Metallurgical and Materials Engineering, 34467 Istanbul, Türkiye. [2]Institut für Werkstofforientierte Technologien – IWT, Badgasteiner Straße 3, 28359 Bremen, Germany. [3]Photon Science, Deutsches Elektronen-Synchrotron DESY, Notkestr. 85, 22607 Hamburg, Germany. [4]National Taiwan University, Department of Materials Science and Engineering, Roosevelt Road, Taipei 10617, Taiwan. [5]Ovako Corporate R&D, Maxwell Centre, JJ Thompson Avenue, Cambridge CB3 0HE, UK. [6]Ovako Corporate R&D, Building 202, SE-813 82 Hofors, Sweden. ✉email: cornek@itu.edu.tr

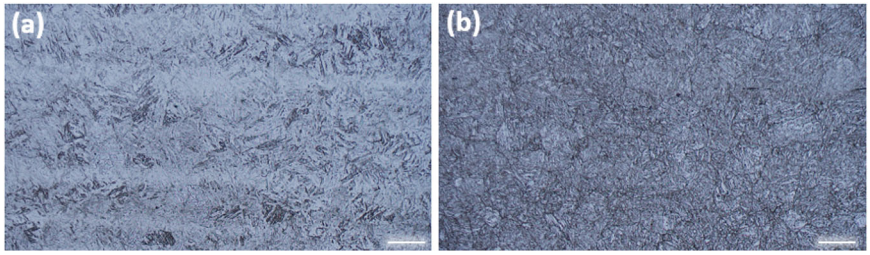

Fig. 1 Optical micrographs showing the microstructure of the Hybrid steel. Left (**a**) is the as-rolled microstructure, and right (**b**) is the tempered condition seen. The specimens were etched with Vilella's etchant. The uneven etching contrast observed in the as-rolled state is due to the effect of elemental segregation during solidification. The length of the scale bar is 60 µm for both micrographs.

secondary carbides and nickel aluminides, which are homogeneously dispersed within the steel matrix[18].

The work aims to understand why *Hybrid* steel, with a concentration of 5 percent of Cr, can show passive-like behaviour in low-pH sulfuric acid and chloride-containing aqueous solutions similar to 420 martensitic stainless steel with 14 weight percent of Cr. The further aim is to understand the passive film formed on *Hybrid* steel and what makes it resistant to chloride corrosion.

RESULTS

Microstructure

The microstructure of the studied *Hybrid* steels is shown in the optical micrographs in Fig. 1. Both microstructures are apparent from the martensitic lath structures. The tempered microstructure contains finely-dispersed carbides and nickel aluminides. Electron microscopy or atom probe tomography can only observe these precipitates[18]. The as-rolled *Hybrid* 55 steel has a hardness of 35 HRC, which increased to 55 HRC by tempering.

The alloy addition of *Hybrid* steel with a carbon content of 0.18 wt.-% promotes the martensitic microstructure after cooling from hot rolling or after solution annealing. Furthermore, the displacive nature of the martensitic transformation enables all the elements formerly in the solid solution in the austenite phase to remain in the martensite after the phase transformation, as there is no diffusion of atoms and the homogenous distribution of all the atomic elements is maintained. During the tempering (or ageing) treatment, vanadium-rich-MC carbides, chromium-rich M_7C_3 and NiAl are formed. In contrast, the martensite lath formed during cooling remains intact (Fig. 2). The precipitation process promotes heterogeneous alloy distribution and decreases the total amount of chromium and aluminium within the matrix (Figs 2, 3). The Cr-rich M_7C_3 carbides are 20–50 nm large and form on lath boundaries of martensite (Fig. 3a, b). Vanadium-rich MC carbides with NiAl precipitates are 5–10 nm in size and are preferably unclear within the lath. Vanadium-rich carbide holds the Baker-Nutting orientation relationship with the martensite matrix (Fig. 3d, e)[19]. It is confirmed that Vanadium-rich carbide is NaCl-structured MC carbide. NiAl compounds undergo ordering transformation and hold a cube-on-cube orientation relationship (Fig. 3d, f)[20]. The microstructure shows some segregation of chromium, nickel and molybdenum (Fig. 4).

Electrochemical passivation behaviour in acidic solutions

The potentiodynamic polarization behaviour of the Hybrid steels in de-aerated sulfuric acid is summarized in Fig. 5a, b. The polarization behavior of the stainless-steel specimens, the interstitial free/carbon (IF/C) steel and the pure metals (nickel, chromium, and aluminium) are shown for comparison purposes only. The polarization behavior of stainless steel is well-known in the literature; the discussion is focused on understanding the polarization behaviour of *Hybrid* steel. In de-aerated sulfuric acid (pH 0.5), the as-rolled and tempered *Hybrid* steels show an active-to-passive transition peak and a broad passive region until transpassive breakdown. The critical passivation current density of the as-rolled *Hybrid* steel is higher than the stainless steels but lower than IF steel, indicating an improved passive behaviour compared to IF steel. However, in the pH 3 acidic solution, the IF steel and tempered *Hybrid* steel showed no passivation but spontaneous active dissolution. In contrast, the as-rolled *Hybrid* steel underwent passivation in the same solution after a wide active dissolution during anodic polarization beyond the corrosion potential. The critical passivation current densities for the stainless steel and *Hybrid* steel ranged from 10^{-6} to 10^{-4} A.cm^{-2}.

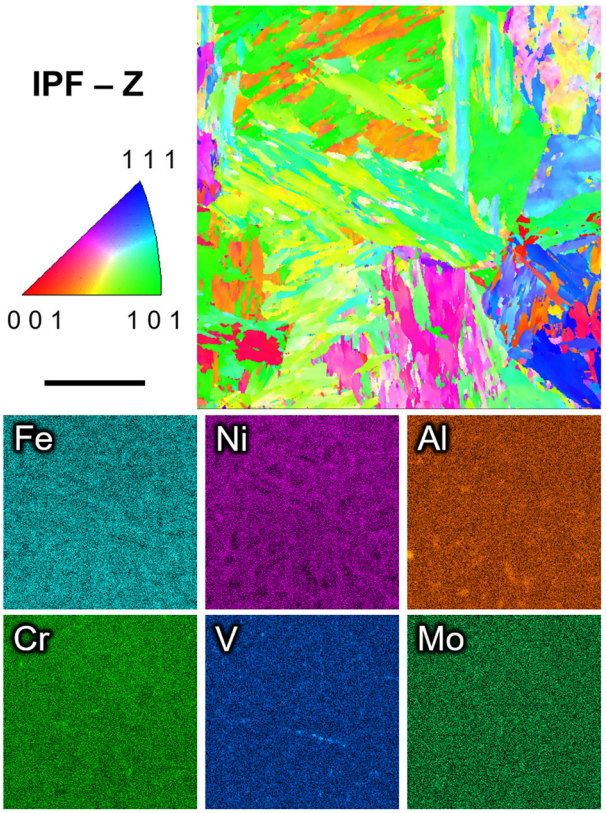

Fig. 2 Crystalographic and chemical information of the microstructure. EBSD-EDS mapping results of the tempered Hybrid steel showing the IPF-Z map in the rolling direction and the corresponding chemical maps of the main alloying elements. The length of the scale bar is 10 µm. The EDS provide chemical information from the inverse pole figure (IPF) map.

The as-rolled *Hybrid* steel showed an extended passive range in the pH 0.5 solution compared to all measured steels, including 304 stainless steel, at high anodic polarization between approximately 900 mV and the water reduction potential (see Fig. 5). In

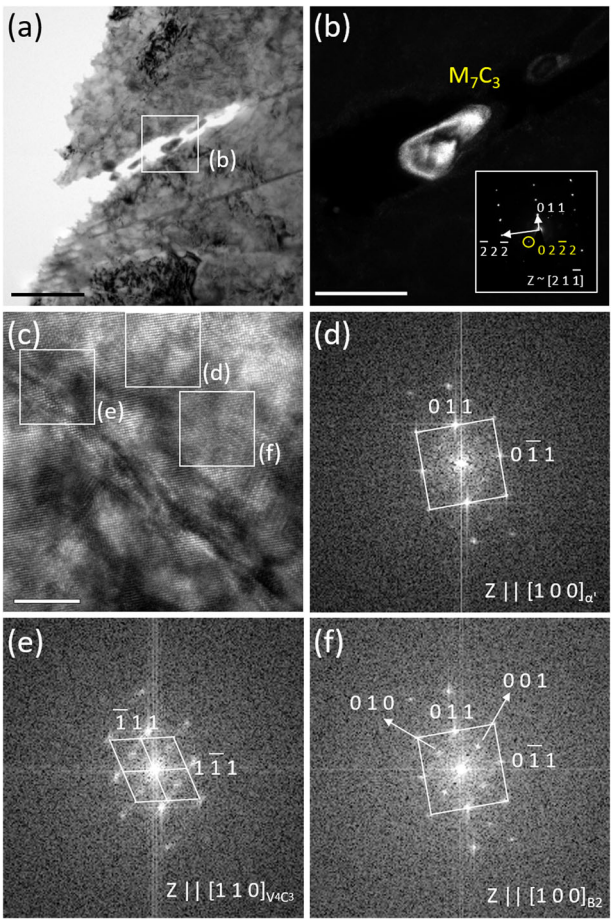

Fig. 3 High-resolution morphological and diffraction information of the microstructure. TEM bright-field image in (**a**) shows the distribution of M_7C_3 carbides, (**b**) a magnified view of the highlighted region in (**a**) with the corresponding electron diffraction pattern, (**c**) shows the distribution of V_4C_3 carbides and NiAl_B2 intermetallic compounds around a dislocation in the tempered martensite, (**d**) the corresponding fast Fourier transform of the martensitic matrix, (**e**) of a V_4C_3 carbide and (**f**) of a NiAl_B2 intermetallic compound. The length of the scale bars is 200 nm, 50 nm, and 5 nm, respectively.

other words, while 304 stainless steel underwent transpassive dissolution at around 900 mV, the as-rolled Hybrid steel remained passive until the water-splitting potential and possibly beyond. The polarization curves showed several peaks as a function of anodic polarization. The activation peak beyond the corrosion potential comprises at least three specific elemental dissolution activities. Electrochemical data read from the polarization curves are summarized in Table 1. The table shows that the passivation potential reduces with increasing alloying content, reducing the passivation current density and the critical passivation current density. Among all tested alloys, only 304 stainless steel showed transpassive breakdown before the water-splitting reaction, apparent from the steep rise of the anodic current density at about 750 mV. The passive film of pure chromium broke at around 750 mV, indicating that the breakdown of chromium oxide in 304 stainless steel is responsible for the passivity. The breakdown of nickel's passive film occurred at about 900 mV suggesting no (significant) contribution to the passivity of stainless steel. The increase of the anodic current density at approximately 1.42 V in the pH 0.5 solution and around 1.33 V in the pH 3 electrolyte suggests the transpassive breakdown of the passive film for the as-rolled *Hybrid* steel. *Hybrid* steel showed extended passivity compared to 304 stainless steel in the pH 0.5 acidic electrolyte. Pure aluminium did not show a steep rise even far beyond the water-splitting potential indicating superior breakdown resistance and sluggish behaviour to oxygen evolution.

Electrochemical pitting tests in chloride-containing solutions

The results of the polarization behavior in the near-neutral chloride solutions are presented in Fig. 6, with the corrosion and pitting potentials listed in Table 2. The as-rolled *Hybrid* steel show similar polarization behavior to the grade 420 martensitic stainless steel. The corrosion current densities at the corrosion potential for each tested steel are on the order of sub-micro to microamps. All tested steels show a steep rise in anodic current density after a few hundred millivolts beyond the corrosion potential. A steep climb in anodic current density in chloride-bearing solutions is a sign of the breakdown of the surface oxide that imparts resistance to anodic oxidation, hence, pitting corrosion. Thus, the polarization curves indicate an existence of a breakdown potential and hence passivity. Since no active behavior was observed, the data suggests spontaneous passivity for the *Hybrid* steels and the martensitic stainless steel. The *Hybrid* steels and 420-steel showed minor current fluctuations close to the breakdown potential, indicating metastable pitting events. The passive current densities of the *Hybrid* steel were on similar levels as the martensitic stainless steel. The latter showed similar breakdown potential to the as-rolled *Hybrid* steel. The polarization behavior of the IF steel showed an immediate rise in anodic current density, indicating spontaneously active corrosion in both solutions. The polarization curves were reproducible, with a maximum deviation of 50 mV.

Corrosion morphology

After the polarization tests in the 0.01 M chloride-containing solution, the corrosion morphology was examined with an optical microscope (Fig. 7). Like the 420 martensitic stainless steel, the *Hybrid* steel showed several corrosion pits in the exposed area, indicating the existence of a protective passive surface oxide and its local breakdown on several sites. The pits on the *Hybrid* steel were hemispherical and dish-shaped, whereas lacy-cover pits with a perforated layer formed on the martensitic stainless steel. Localized corrosion on *Hybrid* steel was also observed in the more aggressive chloride-concentrated solution (Figs. 8, 9). However, the corrosive attack manifested itself in bands, which were more severe in the tempered microstructure. The bands were about 50–100 microns wide and elongated along the rolling direction. The banded corrosion morphology is due to a preferential attack on an elemental deficient region caused by solidification and hot deformation during alloy production, known as micro-segregation[18].

Segregation is a common metallurgical issue in steel production. The segregation can be noticed in the optical micrograph shown in Fig. 1. The compositional variation in the microstructure has been reported in earlier communication[18]. Alloying elements, mainly nickel and chromium, vary perpendicular to the rolling direction. Differences in composition lead to the formation of micro-galvanic cells, becoming more influential with rising corrosion severity. This effect was not seen in the diluted chloride solution. Micro-galvanic corrosion occurs when the corroding region is active while the remaining part is passive, driven by the oxidation power strength of the electrolyte (and polarization). Such a phenomenon is typical, for example, for duplex stainless steel[21]. In earlier work, it has been shown that the corrosion of duplex stainless steel in diluted chloride solution is pitting, which selectively occurs in the ferrite phase[21,22]. The corrosion concentrates more on the entire ferrite phase when the chloride concentration is increased due to more pit nuclei forming next to each other in the ferrite phase with very high density. In this work, the situation is practically the same. Segregated sites

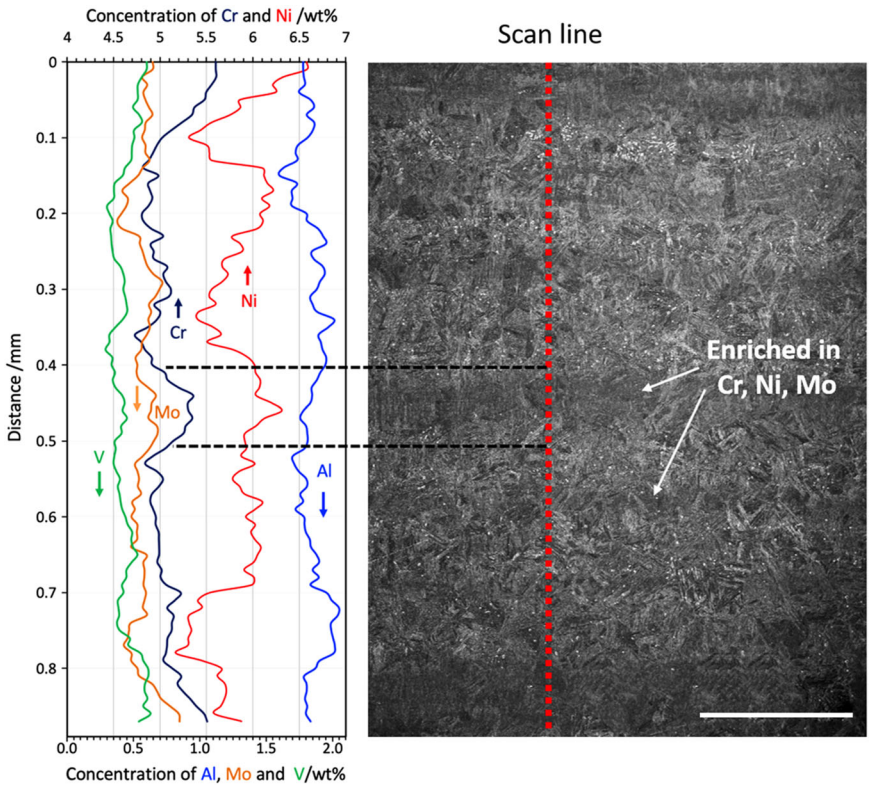

Fig. 4 Microstructural heterogeneity. SEM-EDS line scan analysis result showing elemental segregation in *Hybrid* steel. The length of the scale bar is 200 µm.

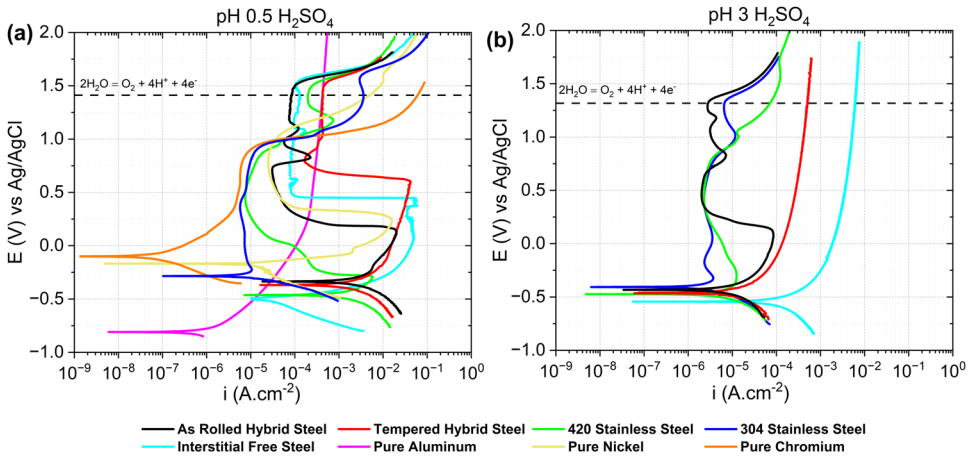

Fig. 5 Electrochemical polarization diagrams in acidic solutions. Potentiodynamic polarization behavior in de-aerated sulfuric acid in (**a**) pH 0.5 and (**b**) pH 3 at room temperature. The dashed line indicates the water-splitting potential calculated using the Nernst equation. The anodic polarization behaviour of the pure metals supports the interpretation of the polarization behaviour of the tested steels. Therefore, tests in pH 3 solution were redundant.

showing more noble alloy composition behave as net cathodes whereas elemental depleted sites become net anodes. Interestingly, despite the high polarization above the breakdown potential, the major corrosion occurred on the segregation bands.

Surface chemistry analysis

To further understand the polarization behaviour of *Hybrid* steel, we performed HAXPES analysis using synchrotron x-ray radiation. We polarized both *Hybrid* steels to various anodic polarization levels, as indicated in Supplementary Fig. 1 and Table 3, to understand why the as-rolled condition showed passivation behaviour and the reason for the minor activation peaks in the polarization curve. The oxidation behaviour of the tempered steel was similar to the low-carbon steel (IF steel). Therefore, only one polarization state was chosen. Specimen no. 1 and no. 6 are non-polarized conditions forming native surface oxide/oxyhydroxide. The survey HAXPES spectra are given in Fig. 10. Several core-level peaks of the alloying elements can be seen. Some Auger peaks are also labelled. The Cr 2p, Fe 2p, Ni 2p, Mo 3p, and O 1 s core level peaks were scanned in high resolution. The Mo 3p core level has been chosen instead of Mo 3d due to better intensity-to-background signal ratios. The Al 1 s core level peaks are not

Table 1. Electrochemical data extracted from the polarization curves presented in Fig. 5.

Electrolyte	Material	Passivation Potential (V vs Ag/AgCl)	Critical Passivation Current (A/cm^2)	Passivation Current (A/cm^{-2})	Transpassive Potential* (V vs Ag/AgCl)
pH 0.5 H_2SO_4	As rolled *Hybrid* steel	0.15	$1{\cdot}10^{-2}$	$3.1{\cdot}10^{-5}$	1.5
	Tempered *Hybrid* steel	0.6	$4{\cdot}10^{-2}$	$1.7{\cdot}10^{-4}$	1.5
	420 stainless steel	−0.31	$6{\cdot}10^{-3}$	$9.4{\cdot}10^{-6}$	1.5
	304 stainless steel	−0.22	$1{\cdot}10^{-5}$	$2.7{\cdot}10^{-6}$	0.75
	Interstitial-free steel	0.45	$5{\cdot}10^{-2}$	$1.1{\cdot}10^{-4}$	1.5
	Pure Chromium	Spontaneously passive		$5.7{\cdot}10^{-6}$	0.75
	Pure Nickel	0.27	$1{\cdot}10^{-2}$	$2.5{\cdot}10^{-5}$	0.9
	Pure Aluminium	Spontaneously passive		$2.6{\cdot}10^{-4}$	No breakdown
pH 3 H_2SO_4	Non-Tempered *Hybrid* steel	0.1	$9{\cdot}10^{-5}$	$2.0{\cdot}10^{-6}$	1.34
	Tempered *Hybrid* steel	Spontaneously active			
	420 stainless steel	−0.30	$1{\cdot}10^{-5}$	$2.7{\cdot}10^{-6}$	1.34
	304 stainless steel	−0.34	$6{\cdot}10^{-6}$	$2.3{\cdot}10^{-6}$	1.34
	Interstitial-free steel	Spontaneously active			

*based on the steep rise of the anodic current density.

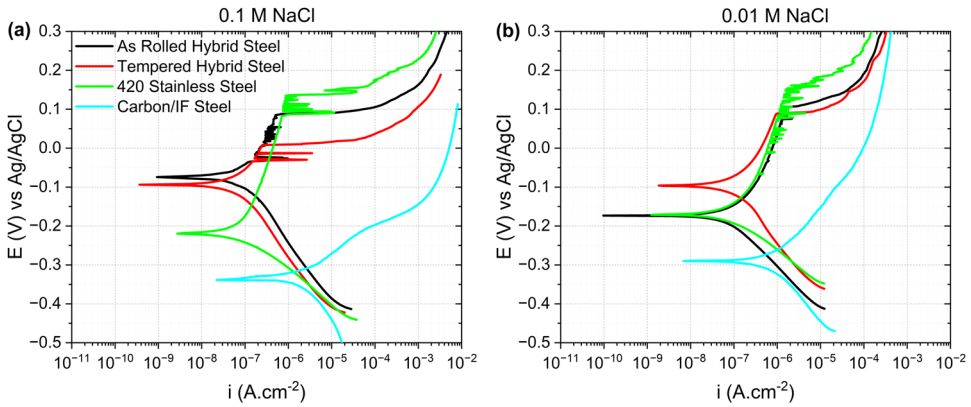

Fig. 6 Electrochemical polarization diagrams in NaCl solutions. Potentiodynamic polarization behavior in (**a**) 0.1 M and (**b**) 0.01 M NaCl solution (near neutral pH) at room temperature. Note that interstitial free (IF) and carbon (C) steel have similar behavior and represent pure iron's behaviour.

shown in the survey spectra, but these were also scanned in high resolution. These gave far more intensity yield than the Al 2p signals and were, therefore, chosen for the high-resolution analysis. The *Hybrid* steel contains minor silicon, which was disregarded in the HAXPES analysis. Samples 6 and 7 showed additional peaks, which were identified as carbides. Tempering produces mainly Cr-rich and V-rich carbides and nickel aluminides (NiAl), which were not distinguishable from the Ni 2p core level spectra. Transition metal carbides can be several tens of eV's away from the carbon core level peak.

The high-resolution HAXPES analysis results for the main alloying elements are shown in Fig. 11. The core level peak ratios of the metallic and oxidation states change as a function of anodic polarization and microstructure (Fig. 12). The native oxide of *Hybrid* steel is composed of Fe, Cr, Ni, Mo, and Al oxides/oxyhydroxides. The as-rolled steel contained considerably more aluminium and nickel oxide than the tempered steel. The HAXPES results of sample 3 (as-rolled) and sample 7 (tempered) show that the surface chemistry evolved after polarization to 500 mV vs Ag/AgCl (see Table 3 and Supplementary Fig. 1). Thus, the aluminium and chromium oxide species are mainly responsible for the passivation of the as-rolled *Hybrid* steel. The HAXPES fitting results for each peak model defining the composition of the surface film of *Hybrid* 55 steel are listed in detail in Supplementary Table 1.

Furthermore, it is essential to note that inelastic background effects play a significant role in HAXPES measurements of stacks and (deeply) buried layers[23]. The peak intensities and the background of inelastically scattered electrons are linked together through the depth distribution of atoms in complex samples. Therefore, background analysis can significantly increase the capabilities of HAXPES to more accurately determine the composition and structure of surfaces and buried layers.

Thermochemical modelling for Hybrid steel in acidic solutions

The thermochemical modelling results are given in Figs. 13, 14, 15. Figure 13a shows the calculated phase diagram section for the H_2O – O_2 – H_2SO_4 – Steel system (four components). 'Steel' is the chemical composition of *Hybrid* steel but as the sum of aqueous ionic and solid compound products. The diagram shows the formed solid corrosion products and their molalities (y-axis) as a function of added metal concentration (x-axis) at initial pH 0.5 with a fixed oxygen partial pressure of 10^{-1} atm. The oxygen partial pressure has a nearly linear relationship (see Fig. 13b) with the redox potential of the steel-electrolyte system. Therefore, 10^{-1} atm oxygen partial pressure was deliberately chosen to

Table 2. Electrochemical data extracted from the polarization curves presented in Fig. 7.

Electrolyte	Material	Corrosion Potential (V)	Pitting Potential (V)
0.1 M NaCl	As rolled *Hybrid* steel	−0.07	0.08
	Tempered *Hybrid* steel	−0.09	0.00
	420 stainless steel	−0.21	0.13
	Interstitial-free steel	−0.33	Spontaneously active
0.01 M NaCl	Non-Tempered *Hybrid* steel	−0.17	0.10
	Tempered *Hybrid* steel	−0.09	0.09
	420 stainless steel	−0.17	0.16
	Interstitial-free steel	−0.28	Spontaneously active

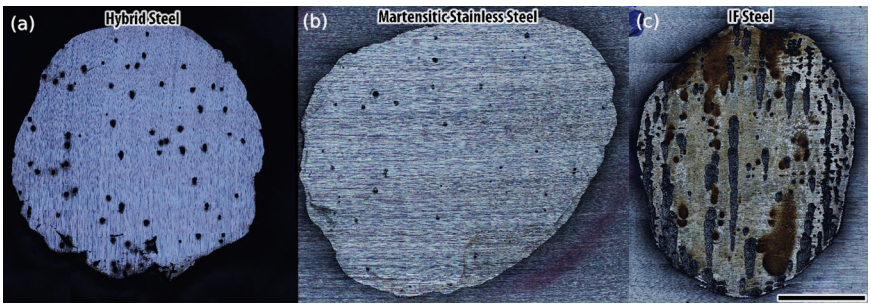

Fig. 7 Corrosion morphology after electrochemical polarization. Optical micrographs showing the corrosion morphology of the (**a**) as-rolled *Hybrid* steel, (**b**) 420 martensitic stainless steel, and (**c**) IF steel after the potentiodynamic polarization experiments in 0.1 M NaCl. Discrete corrosion pits were formed in the *Hybrid* and martensitic stainless steels. In addition, several lacy-cover pits formed in 420 stainless steel. The specimens were masked with a crevice-tight epoxy resin before the polarization experiments. The length of the scale bar is 3 mm and applies to all figures.

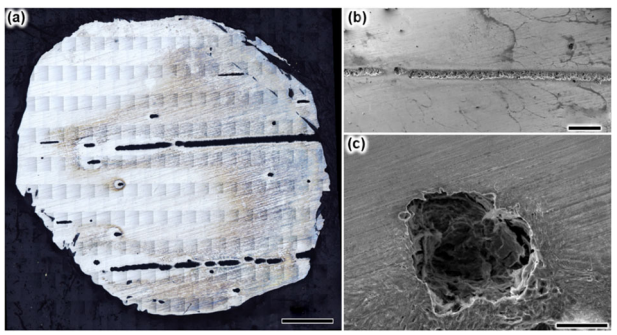

Fig. 8 Corrosion morphology after electrochemical polarization. Corrosion morphology of as-rolled *Hybrid* steel after potentiodynamic polarization in 0.1 M NaCl solution. **a** Optical micrograph showing the entire exposure area where discrete corrosion bands formed, **b** SE-SEM image showing the banded corrosion structure in higher magnification, and (**c**) SE-SEM image showing a corrosion pit. The length of the scale bars are 1200 µm, 500 µm, and 30 µm, respectively.

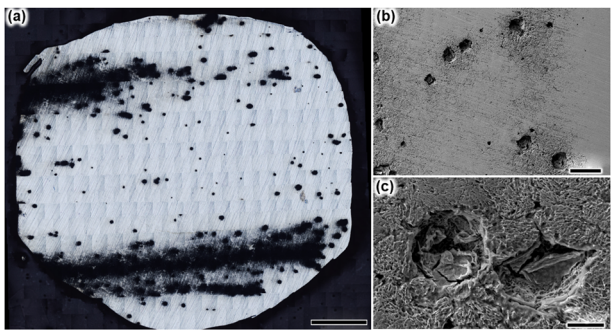

Fig. 9 Corrosion morphology after electrochemical polarization. Corrosion morphology of tempered Hybrid steel after potentiodynamic polarization in 0.1 M NaCl solution. **a** Optical micrograph showing the entire exposure area with discrete banded corrosion structures and corrosion pits and (**b**, **c**) SE-SEM image showing corrosion pits and attack on the martensitic matrix with higher magnification. The length of the scale bars is 1200 µm, 100 µm, and 20 µm, respectively.

reflect the polarization curve (around 1.3 V in Fig. 5) at high anodic potentials ('High Potential'). Figure 13a shows that Fe_2O_3 forms at lower metal cation concentrations in the electrolyte (the system described above), followed by $NiSO_4(H_2O)_7$ and then $Al_2O_3(H_2O)$. The formation of the latter two products requires more metal dissolution, hence, more (intense) polarization. So, at high potentials, these products are thermodynamically stable, and at least these contribute to the passivity of *Hybrid* steel.

It should be noted that the modelling results only represent a local equilibrium that takes a 'long' polarization time and ignores kinetic considerations. The x-axis represents the metal concentration in the local equilibrium, which includes all of the metal-oxide compounds assumed to be formed on the steel electrode and metallic cations and anions in the electrolyte. Figure 13c shows that the interfacial pH change drastically increased with the metal cation concentration. The minor interfacial pH change at low metal ion concentration is due to the formation of Fe_2O_3. The oxygen needed for iron oxide formation is delivered primarily from water molecules, resulting in dissociation and hence a rise in pH. The interfacial pH increases sharply when nickel sulphate and aluminium oxide are formed. Furthermore, the sharp rise in pH is associated with the amount of Fe_2O_3 and the formation of

Table 3. The specimens used for HAXPES analysis.

Sample	Material Condition	Polarization Condition (vs Ag/AgCl) in sulfuric acid	Explanation
1	As-rolled	–	Reference state
2	As-rolled	100 mV	Highest metal dissolution
3	As rolled	500 mV	Quasi-passive state
4	As rolled	800 mV	Minor removal of the passive layer
5	As rolled	1100 mV	Further minor dissolution of the passive layer
6	Tempered	–	Reference state
7	Tempered	500 mV	Oxidation state far above the OCP (no passivity)

The samples were polarized from OCP until the given potential. The surface of the non-polarized conditions has native oxides/hydroxides.

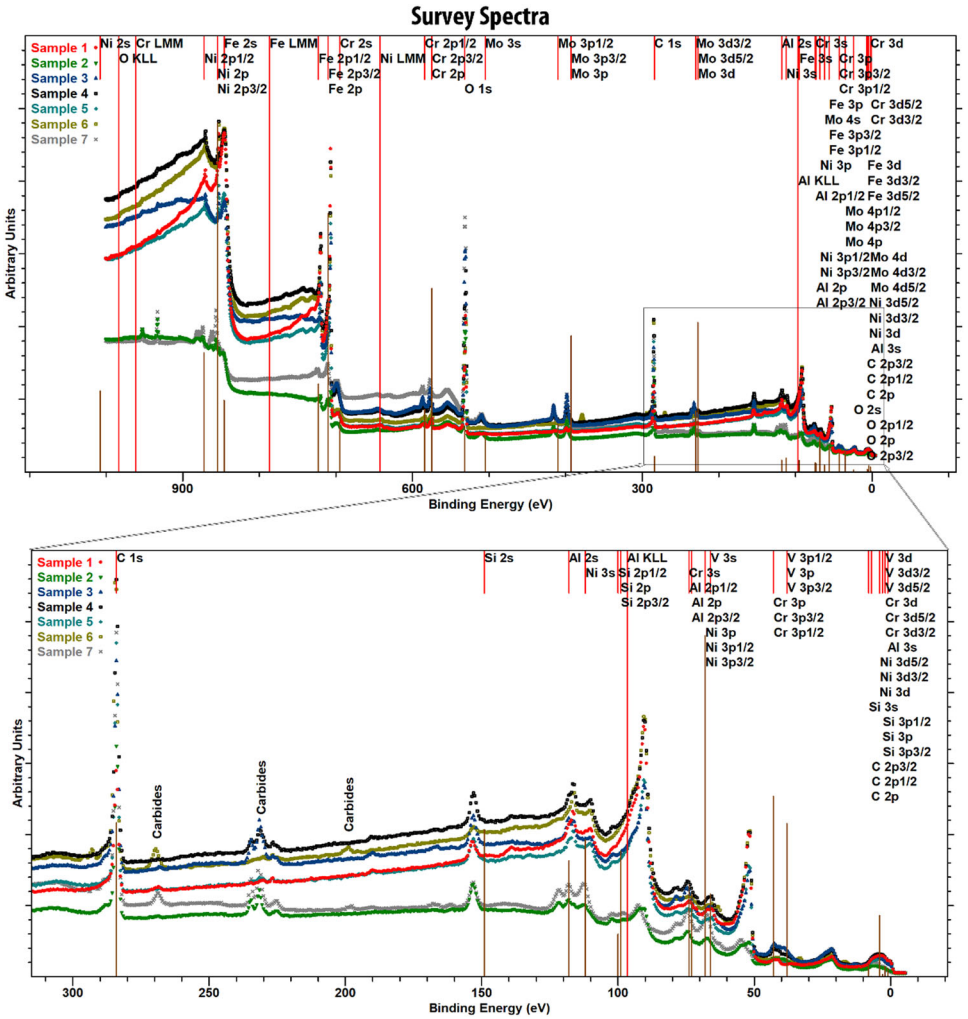

Fig. 10 Surface chemistry information. Survey HAXPES spectra for each sample as specified in Table 3.

$NiSO_4(H_2O)_7$ and $Al_2O_3(H_2O)$ due to water dissociation and crystalline water bound to each product molecule. No chromium oxide exists when the redox potential is high enough to dissolve chromia.

The corrosion products formed at low redox potential are depicted in Fig. 14. 'Low' in this context represents the passive state of the polarization curve of *Hybrid* steel (at around 500 mV in Fig. 5). The modelling results show that Fe_2O_3, $NiSO_4(H_2O)_7$ and $Al_2O_3(H_2O)$ form first during polarization, followed by the production of Cr_2O_3 and $(NiO)(Fe_2O_3)$. It should be noted that the latter compound could have also been calculated as NiO. So, the oxide product shall be understood as nickel oxide. We disagree with the classic understanding that surface oxides are layered or stratified. However, there is a chemical gradient along and across the surface film in all geometrical dimensions. All oxides build together one complex film entity on the surface. Compared to high potentials, chromia and nickel oxide are stable at low potentials. Therefore, the formation of chromia increases the interfacial pH, like iron, nickel, and aluminium products. A steep rise in pH occurs when $(NiO)(Fe_2O_3)$ forms, shifting the interfacial pH by more than two orders of magnitude. These explain the passive behaviour of *Hybrid* steel in de-aerated pH 0.5

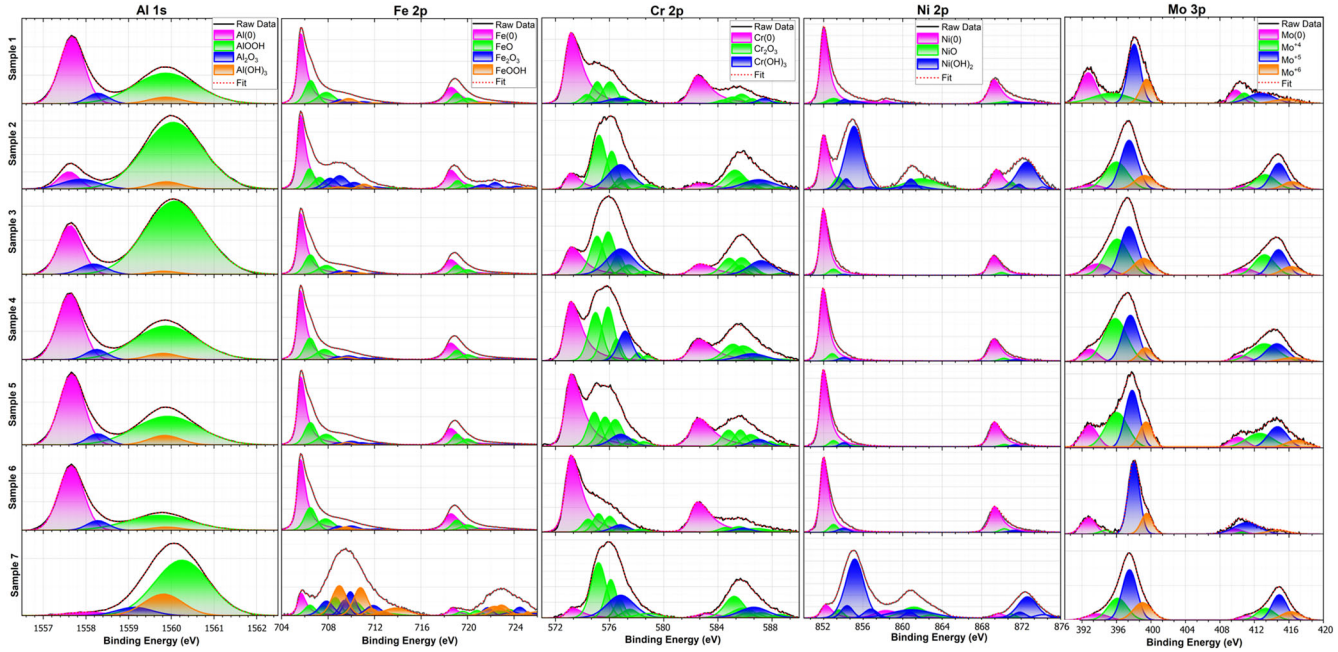

Fig. 11 Surface chemistry information. High-resolution HAXPES spectra of Al 1 s, Fe 2p, Cr 2p, Ni 2p, and Mo 3p core levels for the samples as specified in Table 3.

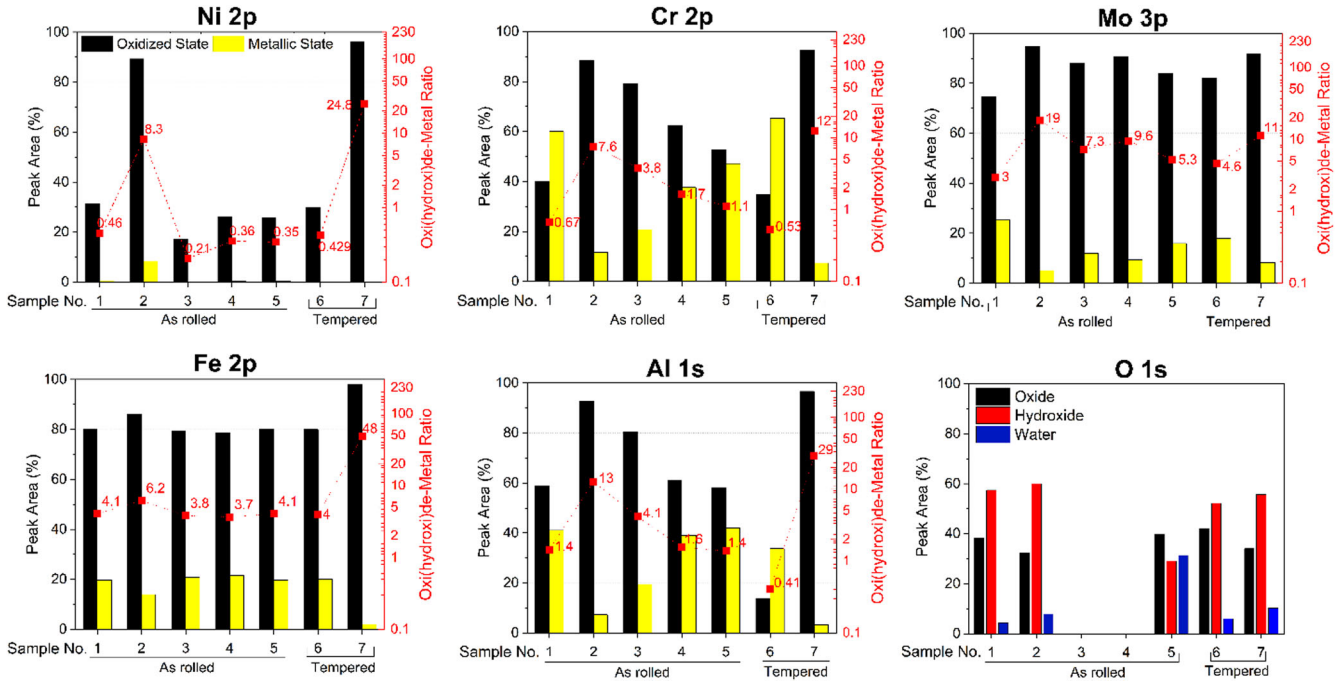

Fig. 12 Surface chemistry information. Semi-quantitative HAXPES results. The surface composition changes qualitatively as a function of microstructure and anodic polarization.

sulfuric acid solution. The steepest rise in pH occurs when (NiO) (Fe_2O_3), a spinel-type oxide, forms, indicating a significant contribution to passivity.

The computational modelling results are summarized in Fig. 15a, showing the formed corrosion products and their molalities as a function of oxygen partial pressure (fugacity) in pH 0.5 sulfuric acid solution. The x-axis (logarithmic oxygen concentration) can be qualitatively understood as the Eh of a classic Pourbaix diagram and the redox potential of a standard electrochemical polarization curve. Oxygen pressure on the order of 10^{-50}–10^{-60} atm is highly deficient and indicates practically no anodic polarization. So, it can be deduced that the spinel oxides $FeCr_2O_3$, (NiO)(Fe_2O_3), and Al_2O_3(H_2O) form the native oxide of *Hybrid* steel in the acid. The latter two compounds remain stable throughout polarization until the breakdown potential of the Cr(III)/Cr(VI) couple redox potential sets on, which is at about 750 mV in the polarization curve (see Fig. 5).

Figure 15b shows that the oxygen fugacity and the Eh have a nearly linear relationship. With increasing oxygen fugacity

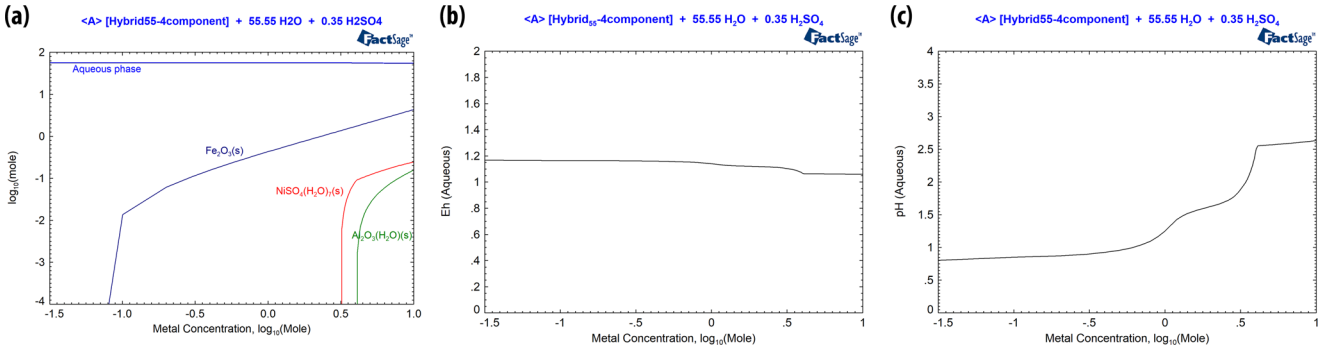

Fig. 13 Corrosion products modelled by thermodynamic calculations. CalPhaD-based thermochemical modelling results in pH 0.5 sulfuric acid solution showing (**a**) the formed corrosion products and their molalities as a function of added metal concentration, (**b**) the redox potential evolution plotted vs system's total metal concentration, (**c**) the pH evolution as a function system's total metal concentration. Note that the products formed and potential and pH changes were calculated for an oxygen partial pressure of 10^{-1} atm, so at 'high' redox potential. The redox potential in (**b**) indicates the strength of what 'high' means.

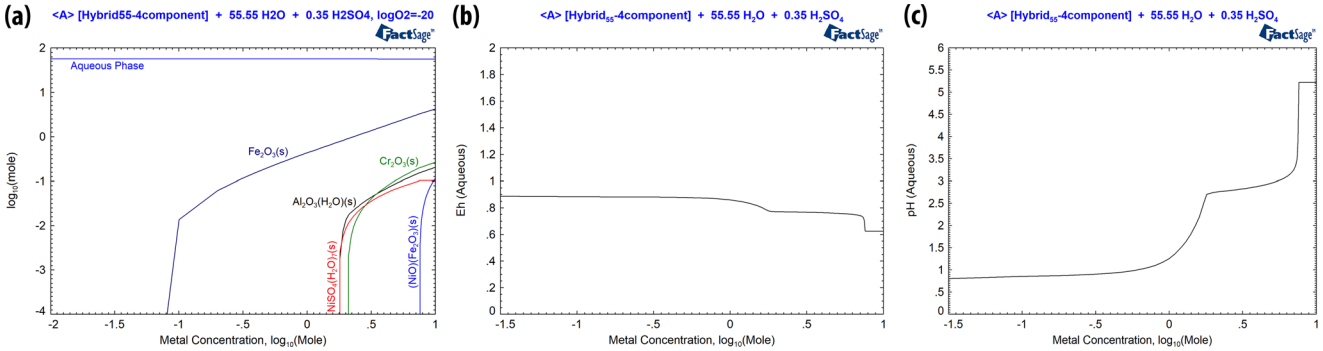

Fig. 14 Corrosion products modelled by thermodynamic calculations. CalPhaD-based thermochemical modelling results in pH 0.5 sulfuric acid solution showing (**a**) the formed corrosion products and their molalities as a function of added metal concentration, (**b**) the redox potential evolution plotted vs system's total metal concentration. (**c**) The pH evolution as a function metal cation concentration. Note that the products formed and potential and pH changes were calculated for an oxygen partial pressure of 10^{-20} atm, so at 'low' redox potential. The redox potential in (**b**) indicates the strength of what 'low' means.

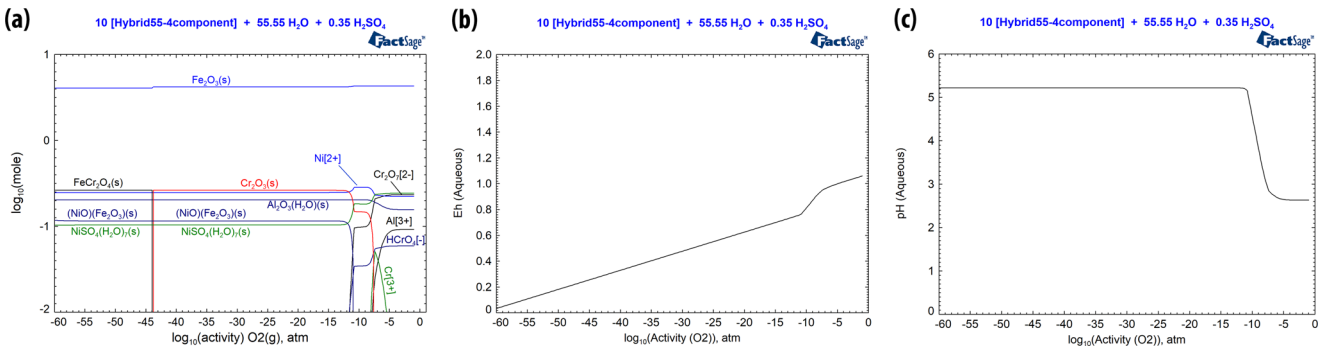

Fig. 15 Corrosion products modelled by thermodynamic calculations. CalPhaD-based thermochemical modelling results show (**a**) the formed corrosion products and their molalities as a function of oxygen partial pressure (fugacity) in pH 0.5 sulfuric acid solution, (**b**) the corresponding potential (Eh) evolution and (**c**) the corresponding pH with changing oxygen fugacity. Note that the products created and potential and pH changes were calculated for a total metal (aqueous and solid compounds) concentration of 10 M in sulfuric acid at bulk electrolyte pH of 0.5.

(≈ electrode potential, Eh), $FeCr_2O_3$ transforms to Cr_2O_3, indicating selective oxidation of iron. As a result, more Fe_2O_3 is produced, forming the most surface oxide. The anodic dissolution of Cr_2O_3 and NiO occurs at similar potentials. The amount of $NiSO_4(H_2O)_7$ increases indicating a conversion of NiO to $NiSO_4(H_2O)_7$. The dissolution of Cr_2O_3 reduces the interfacial pH by more than two orders of magnitude. Thus, producing Cr^{6+} (aq) ions causes severe acidification due to water hydrolysis.

The thermodynamic computation in 0.1 M chloride solution predicts Fe_2O_3, NiO, Cr_2O_3 and Al_2O_3 as the native surface oxide passive film of *Hybrid* steel (Fig. 16). Like sulfuric acid's reaction, $FeCr_2O_3$ transforms to Cr_2O_3, indicating environment-independent behaviour. We performed the calculations with and without CO_2, a typical electrolyte compound due to its ubiquitous presence in the air and its immediate absorption by the aqueous solution. The solution's initial pH was about 6.5, measured before the

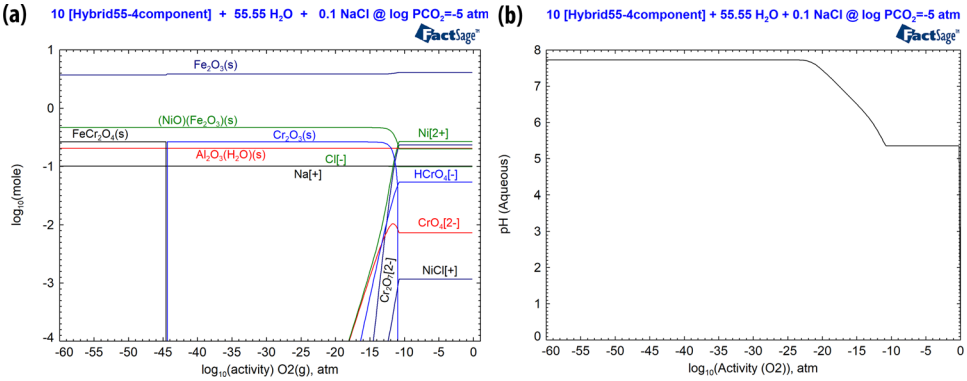

Fig. 16 Corrosion products modelled by thermodynamic calculations. CalPhaD-based thermochemical modelling results show (**a**) the formed corrosion products and their molalities as a function of oxygen partial pressure (fugacity) in 0.1 M NaCl solution that contains some minor CO_2 (natural uptake from the air) and (**b**) the corresponding potential (Eh) evolution and (**c**) the corresponding pH with changing oxygen fugacity. Note that the solution's initial pH before computation but precalculation by the software was 6.4, the typical value of fresh 0.1 M NaCl due to natural acidification by CO_2. After calculation, the system increased the interfacial pH to mild alkaline values. The effect of CO_2 was seen to be minor and hence negligible.

experiment. FactSage showed a pH of 6.4 when we added 10^{-5} atm CO_2 fugacity, and after the simulation, the system's pH (the interfacial pH) became minor alkaline. Hence, the natural presence of CO_2 is insignificant and, therefore, negligible.

The surface is protective until Ni^{2+} (aq) and Cr^{6+} (aq) are formed before the breakdown (dissolution) of NiO and Cr_2O_3. The degradation of the passive film occurs when the molality of the solid oxide compounds reduces in magnitude, especially with the dissolution of Cr_2O_3. It should be noted that the removal of Cr_2O_3 is triggered by the excessive formation of Cr^{6+} (aq), which reduces the interfacial pH by more than two orders of magnitude (Fig. 16). Cr^{6+} ions form several complex molecule ions and have a strong hydrolysis effect. We have calculated the corrosion products with their molalities as a function of oxygen fugacity for pure iron, chromium, nickel, and aluminium. We have seen no pH change except for chromium. The calculations indicate that the pH reduction reasons the dissolution of Cr_2O_3. The lowering of the interfacial pH also dissolves NiO but favours Fe_2O_3 production. Al_2O_3 is only slightly affected by the pH and, therefore, takes a more decisive role in passivity since it remains on the surface.

DISCUSSION

The electrochemical measurements have shown that the *Hybrid* steel shows similar corrosion behavior to grade 420 martensitic stainless steel in de-aerated sulfuric acid and near-neutral sodium chloride solutions. *Hybrid* steel offers passive behaviour and a steep rise in anodic current density (breakdown and even pitting), suggesting a stainless-steel-like character. It is well-accepted that a minimum of 10.5% Cr is needed to render steel stainless. However, *Hybrid* steel contains only 5% Cr; therefore, chromium oxide alone cannot explain its passive-like behaviour. The CalPhaD-thermochemical computation analyses, augmented by the HAXPES results, have shown that other alloying elements participate in the surface oxides, supporting chromium oxide in corrosion protection. Thus, the surface oxide is composed of $Fe_2O_3 \cdot FeCr_2O_4 \cdot NiO \cdot Al_2O_3$, which changes structure, fraction and existence over electrochemical polarization.

Furthermore, the thermochemical modelling has shown that when Cr(VI) species form upon transpassive breakdown of Cr_2O_3, the interfacial pH is reduced, which causes some dissolution of the remaining passive surface oxides. Therefore, *Hybrid* steel could repassivate despite the loss of Cr_2O_3. Furthermore, the computational calculations and HAXPES analyses have shown that Al, Ni and Mo oxides exist beyond the polarization at electrochemical potentials above the transpassive dissolution potential of chromia. Thus, it has become clear that oxides other than chromium oxide contribute to the passivation of *Hybrid* steel.

In this context, aluminium oxide is highly beneficial to *Hybrid* steel. Aluminium oxide forms a dense, potent, sluggish oxide to electron transfer reactions. Hybrid steel exhibits passive behavior in both heat-treated conditions, as apparent from the polarization behaviour in acid and chloride solutions. The nickel cations in the oxide must also benefit the steel due to the lower passive currents after the secondary passivation (Fig. 5). It is not true that only iron oxide contributes to the passivity of *Hybrid* steel since the passive currents were consistently lower than that of IF steel (≈ pure iron). The fraction (and its contribution to passivity) of nickel oxide/oxyhydroxide is perhaps the least among all other oxides. Still, the presence of a noble element in the passive film contributes apparently to the corrosion resistance. Its weak contribution of nickel cations to the passive film's structural integrity is also apparent from the third activation peak, which is associated with the loss of nickel due to anodic dissolution from the oxide. *Hybrid* steel could again repassivate with a minor rise in the passive currents, explaining the contribution of nickel to the passivity. Particular emphasis on the contribution of passivity must be given to aluminium. It provides continuous support to the iron oxide, explaining the passive nature of the steel. Our work indicates that the mixed oxides provide a synergism providing exceptional passive behaviour. Some other electrochemical characteristics of what makes steel stainless will be discussed in further detail.

Oxide/Hydroxide formation

The passivity of metals results from the construction of oxide or hydroxide films in the reaction of metals with water. The passivation process has a solid-state reaction mechanism in which the metal is hydrolyzed by water forming a metal oxide complex with the liberation of free electrons and hydronium ions.

$$nM + mH_2O \rightarrow M_nO_m + 2mH^+ + 2me^- \quad (1)$$

The reaction can also be precipitation, according to Lewis, in which metal cations form with a metal hydroxide:

$$M^{z+} + nH_2O \rightarrow M(OH)_z \cdot (n-z)H_2O + 2H^+ \quad (2)$$

The reaction rate is determined by charge transfer. So, with increasing anodic polarization, metal cationization (oxidation) increases. The dissolution kinetics in sulfuric acid solutions assume a Tafel behaviour for active metals like steel. The metal cations hydrate, and metal hydroxides chemisorb and physisorb onto the active metal. These processes are seen on the polarization curves

Table 4. Chemical composition (wt.-%) of the materials investigated.

Material	C	Si	Mn	P	S	Cr	Ni	Mo	V	Al	Cu	Co	Fe
Hybrid 55	0.18	0.1	0.3	< 0.015	< 0.001	5	5	0.7	0.5	2	-	-	Bal.
304 Stainless Steel	0.03	0.6	1.03	0.03	0.006	18.6	7.65	0.04	-	0.007	0.05	0.05	Bal.
420 Stainless Steel	0.3	0.5	0.42	0.02	0.004	14.1	0.12	0.03	-	0.006	0.02	0.02	Bal.
Interstitial-free Steel	0.0068	0.0029	0.018	-	-	0.0008	-	-	-	-	-	-	Bal.
Carbon Steel	0.05	0.01	0.15	0.01	0.02	0.04	0.04	< 0.002	-	0.046	0.02	0.006	Bal.

for the investigated steel alloys as an intense activation peak (Fig. 5). Here, mainly iron but also other alloying elements dissolve with different kinetics. In the passive range, dehydration and dehydroxylation of the film occur, resulting in a thinner and denser oxide, hence, protective[14]. The surface oxide is a mixed oxyhydroxide of varying composition across the depth and lateral space also changing with time[5,7,9,14].

The anodic polarization results show that the *Hybrid* and martensitic stainless steel show an activation-controlled behaviour in the active region in sulfuric acid[24]. Thus, all measured steels in sulfuric acid showed active behaviour, having different dissolution magnitudes. The passivation current dropped with the chromium content in the alloy, and the nickel content shows the most significant effect in austenitic stainless steel, typically reducing the dissolution kinetics of steel[25,26]. IF steel spontaneously corrodes in neutral chloride solutions due to the absence of protective surface oxide. In contrast, stainless steels are often spontaneously passive in these solutions, indicating the necessity of the local breakdown of a passive protective layer to initiate pitting.

No Tafel fitting of the polarization data of *Hybrid* steel was possible in chloride solutions, telling that the corrosion process must have happened under mixed control. Some elements in the alloy system contribute to mass control dissolution kinetics. Iron dissolution occurs under activation control, but the enrichment of the alloying elements slows the iron oxidation explaining the non-Tafel behaviour. The slower oxidation kinetics indicates a protective surface layer, indicating passivity. Lower dissolution kinetics for iron in Fe-Al alloys has been reported[27]. So, the results have shown that *Hybrid* steel offers a stainless character. The alloy composition of the *Hybrid* steel produces a protective passive-like oxide that renders passivity upon anodic polarization. Hence, the steel can passivate and provide exceptional corrosion resistance similar to 14 wt.-% Cr martensitic stainless steel.

Moreover, metastable pit activities were observed in *Hybrid* steel, as apparent from the current spikes in the anodic regime, typical for stainless steel, such as grade 420[28,29]. These features distinguish stainless steel from non-stainless steel. We aim not to extend the discussion but to answer why *Hybrid* steel offers stainless-steel-like polarization behaviour. We conducted electrochemical tests, including impedance spectroscopy and long-term open-circuit potential measurements in various acids and chloride-containing media (results not shown). In all tests, *Hybrid* steel showed similar results to 420 martensitic stainless steel.

Anodic polarization changes the oxyhydroxide-to-metal ratio of the passive film. According to Eq. (2), the surface oxide contains hydrated complexes, which explain the water component in the O 1 s signals of the HAXPES data. It has been reported that the water component is a part of the oxide and increases toward the oxide interior[14]. The presence of water in the oxide has been suggested to be due to the reduction of sulphuric acid[14]. The surface film forms first as a hydroxide but transitions gradually into oxide, hence an oxyhydroxide[10,14]. However, deep in the surface film, the hydroxide content is dominant over the oxide phase. We have not detected sulphate or any sulphurous compounds in the surface film. Such compounds typically form when polarized for long times at high potential, which was not the case in our studies[14,15].

The formation energies of oxides in an alloy dictate the magnitude of metal oxidation and their ratio. The oxide formation energy per oxygen molecule is lowest for Al_2O_3 (−10 eV), followed by Cr_2O_3 (−6.5 eV), then iron oxides [FeO (−3.5 eV), Fe_2O_3 (−4.5 eV) and Fe_3O_4 (−5 eV)], and then NiO (−2.5 eV)[30]. A metal oxide's formation energy describes the metal's affinity to oxygen, providing a quantitative measure for the driving force of oxidation. Since aluminium oxide has the lowest formation energy, its presence in the surface film as oxide or oxyhydroxide is ubiquitous. Chromium oxide has the second lowest formation energy (second strongest formation tendency), which explains its dominating presence in chromium-containing steel. Aluminium oxide is omnipresent and provides a barrier for charge transfer, hence, corrosion resistance. The presence of nickel oxide in the surface film is beneficial since it has lower dissolution kinetics than iron and chromium[25,26]. Molybdenum also provides a protective barrier against metal dissolution, mainly iron, in the form of ferrous and ferric cations[5]. The formation energies for the oxides of the alloying elements explain the mixed metal oxide formation on *Hybrid* steel. In addition, Al_2O_3, Cr_2O_3 and Fe_2O_3 have the same crystal structure with the space group of $R\bar{3}c$. These structures are sometimes called corundum and are named after the high-temperature modification of alumina. The oxygen anions in corundum are hexagonally close-packed. Aluminium, chromium and iron cations occupy two-thirds of the available octahedral sites[31]. The same crystal structure of these oxides indicates that Fe, Al and Cr atoms are interchangeable when the protective oxide layer is formed.

Implications and final remarks

Hyrbid steel is not designed to be used in acidic environments. The polarization experiments in acidic solutions were conducted to characterize and understand the passive layer nature of the *Hybrid* steel. Our work has shown that *Hybrid* steel offers exceptional corrosion resistance and allows comparison to low-alloyed stainless steel. It suggests that steel can be made stainless with a diligent alloying recipe without excessive chromium concentration. Sustainable materials must be corrosion-resistant at affordable costs. Whether *Hybrid* steel can be declared stainless steel or not (or corrosion-resistant steel), the work has shown that tomorrow's stainless steel will be manufactured with precise alloying of elements contributing to passivity. Regarding the corrosion-resistance-to-cost ratio, the work suggests that a mixed oxide with a similar metal cation fraction may outperform a passive with chromium oxide only.

METHODS

Materials used

The material investigated was *Hybrid* 55 steel (Hy55) produced by Ovako AB (Sweden). Its chemical composition is shown in Table 4. In addition, interstitial-free (IF), carbon (C) steel, 304 austenitic stainless steel, 420 martensitic stainless steel, pure aluminium, pure nickel and pure chromium were investigated for comparison. *Hybrid* steel was investigated in two different conditions to

understand the microstructure effect on the corrosion behaviour: (i) as-rolled and solution-annealed (*as-rolled* in due communication) and (ii) as-rolled and tempered at 575 °C for one hour (*tempered* in due communication). In the as-rolled condition, no carbides and other precipitates are expected since the steel was reheated to 1200 °C before hot rolling. However, due to the high hardenability, a martensitic microstructure is formed during cooling to room temperature upon hot-roll treatment. The tempered microstructure contains finely-dispersed nanometer-sized secondary carbides and nickel aluminides in the martensitic structure. Specimens in dimensions of 20 mm (length) by 20 mm (width) by 2–5 mm (thickness) were machined and used for electrochemical testing and HAXPES analysis.

Sample preparation

The specimens were mechanically wet-ground using 240-, 400-, and 600-grit SiC sandpapers. Then, the samples were washed with detergent and rinsed with de-ionized water (18 MΩ) and ethanol. Finally, the pieces were coated with epoxy (Duratek 4480 or Teknomarin Era 4000) to leave an exposure area of spherical shape of about $0.6 \pm 0.1\ cm^2$ for the corrosion tests. The exact exposure area was determined by area measurements from optical micrographs using the HIROX digital optical microscope. The Hybrid steels were tested for their corrosion performance and compared with conventional stainless steels, such as 304 austenitic and 420 martensitic grades, C/IF steels and pure metals (chromium, nickel, and aluminium). Despite distinct material types, IF and carbon steel exhibit strikingly similar properties that closely approximate pure iron's behaviour. Therefore, the properties of interstitial free steel and carbon steel should be considered as a manifestation of pure iron's characteristics. The corrosion experiments were performed in de-aerated sulfuric acid (pH 0.5 and pH 3) to characterize passivation and understand the surface nature of *Hybrid* steel. The latter is a well-known classic test in the corrosion community for describing iron passivation as a function of chloride-free acidic pH[32].

Then, we polarized the *Hybrid* steels to varying anodic potentials (details will be shown later) and performed synchrotron hard X-ray photoelectron spectroscopy (HAXPES) measurements to characterize the surface oxide nature. Furthermore, we performed detailed thermochemical modelling and further simulated the aqueous corrosion behaviour in various electrolytes to understand the surface oxides and possible corrosion products. We completed the computational analyses in different acidic pH with and without chlorides but reported here only a summary. Finally, we augmented our corrosion tests with potentiodynamic electrochemical testing in aqueous chloride solutions to characterize the *Hybrid* steel's corrosion resistance in a chloride-bearing environment, which has the most practical importance. After validating our computational work, we were confident that our model predicts the surface nature of *Hybrid* steel chloride solutions.

Microstructure characterization

The microstructure of the tempered *Hybrid* steel was characterized using electron microscopy, electron backscattering diffraction (EBSD) and X-ray energy-dispersive spectroscopy (EDS). Scanning electron microscopy (SEM), EBSD and transmission electron microscopy (TEM) analyses were performed on the aged (tempered) condition to characterize the intermetallic precipitates. The JEOL JSM-7800F Prime equipped with a NordylsNano EBSD detector and an Oxford X-MaxN X-ray energy-dispersive spectrum (EDS) detector were used for SEM/EBSD/EDS analyses. The EBSD experiments were performed at an operating voltage of 20 kV, a working distance of 15 mm, and a step size of 80 nm, with simultaneous chemical mapping. The investigated specimen was grounded on silicon carbide (SiC) paper to #2500 mesh and twinjet-polished at 20 mA for 1 min in a solution of 5 vol.-% perchloric acid, 15 vol.-% glycerol, and 80 vol.-% alcohol. The formed intermetallic particles (M_7C_3, NiAl B2, and V_4C_3) were characterized using the FEI TECNAI G2 F20 FEG transmission electron microscope (TEM), operated at 200 kV. The TEM foils were prepared by electrochemical twinjet polishing at 38 V in a 5 vol.-% perchloric acid solution, 15 vol.-% glycerol and 80 vol.-% alcohol.

Electrochemical Tests

The electrochemical tests consisted of potentiodynamic polarization in (i) de-aerated sulfuric acid (pH 0.5 and pH 3) and (ii) 0.01 M and 0.1 M NaCl solutions, all carried out at room temperature (25 °C ± 2). The experiments in acidic solutions were explicitly conducted to understand the nature of the surface oxides and the passivation ability of *Hybrid* steel as a function of microstructure and solution pH. In addition, the anodic polarization in the far passive regime was done to characterize the nature of the anodically grown surface oxides. The tests in sulfuric acid were done by de-aerating oxygen from the electrolyte using a continuous stream of high-purity nitrogen gas. The measurements in chloride solutions were done to mimic the corrosion behaviour for most engineering application conditions. The *Hybrid* steel contains chromium and aluminium and is expected to form chromia and alumina surface layers with nanometre thickness. These are known for showing passive properties. Therefore, exposure tests in sulfuric acids were performed to understand whether the steel microstructure influences the passivity. The polarization behaviour of an alloy is dictated by each element's reversible electrochemical potential, which in sum, forms the corrosion potential. Therefore, we tested pure metals in the acidic solutions to understand the *Hybrid* steel's passivation behaviour.

The Gamry Interface 1010E potentiostat was used for all electrochemical tests. The conventional three-electrode setup was employed, with a reference electrode (Ag/AgCl (sat.) or Cu/$CuSO_4$) and a Pt-mesh counter electrode. The specimen served as the working electrode. For the electrochemical tests, an electrochemical cell was manufactured from polyoxymethylene (Delrin). The electrochemical cell and setup can be seen in Supplementary Fig. 2. The electrolyte volume used for all experiments was about 185 ml. Open circuit potential measurements were conducted for 10 min before the polarization tests, reaching near-steady state conditions according to the ASTM G5-14 standard (deviation was less than 10 mV/min, see Supplementary Figs. 3, 4). Potentiodynamic polarization was done by sweeping the electrochemical potential from about −300 mV below the final OCP to 1500 mV vs the reference electrode. The Ag/AgCl reference electrode was used for the measurements. In addition, the Cu/$CuSO_4$ electrode was used in sulfuric acid solutions to ensure no chloride-leakage artefact in the passivation behavior. The sweep rate for all polarization tests was 1 mV/s. All electrochemical tests were conducted at room temperature and repeated a minimum of thrice to confirm repeatability. The data were plotted with the software OriginLab version 2022b.

Corrosion morphology analysis

The specimens were inspected for corrosion morphology using optical microscopy and SEM after the electrochemical tests.

Surface chemical analysis

Synchrotron hard X-ray photoelectron spectroscopy (HAXPES) was employed to characterize the surface chemistry and their energy states with high sensitivity and precision. The main benefit of synchrotron HAXPES is the extraordinarily high beam flux which allows analysis with ultra-high sensitivity, which was needed for detecting nickel. The motivation for using HAXPES was to understand the *Hybrid* steel's surface changes after electrochemical polarization

in a corrosive electrolyte. The steel surface comprises complex oxides/oxyhydroxides of about a few nanometres in total. The wet-ground specimens were utilized for the HAXPES analysis in the condition given in Table 3. The HAXPES analyses were performed at Deutsches Elektronen-Synchrotron (DESY) beamline P22[33]. The analyses were done between 3 and 4 weeks after the sample preparation/polarization giving sufficient time to oxidize the surface to reach a near-steady state condition. The electron spectrometer used was the SPECS Phoibos 225HV hemispherical analyzer. The samples were mounted on a high-precision five-angle Omicron manipulator with a liquid helium cooling system. The excitation energy used was 6000.55 eV. The survey scans were recorded with a constant pass energy of 50 eV. The core level peaks for Fe 2p, Ni 2p, Cr 2p, Mo 3p, O 1 s, and Al 1 s were measured with a pass energy of 30 eV resulting in an energy resolution of 230 meV. The binding energy scale was calibrated with the Au $4f_{7/2}$ line from a gold specimen that was measured with the samples. First, a survey scan between 1200 and 0 eV was performed. Then, we examined the binding energies of the Fe 2p, Ni 2p, Cr 2p, Mo 3p, O 1 s, and Al 1 s core levels with high resolution. These were done to capture all multiplets and subtract backgrounds. The data are shown in reference to the Au $4f_{7/2}$ line (83.98 eV, see Supplementary Fig. 5).

The HAXPES spectra were analyzed with CasaXPS Version 2.3.23PR1.0 software. The peaks were processed using a Shirley background subtraction and fitted based on established models from surface and corrosion science literature[34,35]. The multiplet effect of transition metal oxides and satellite peaks was introduced in the fitting. Notably, the multiplet effect was considered in the peak fitting of the nickel, iron, and chromium oxides. A mixed Lorentzian and Gaussian distribution function was utilized for the oxide and hydroxide peaks, with a Gaussian (70%) and Lorentzian (30%) distribution ratio. Asymmetric peak shapes were employed for metallic peaks. The doublet ratio for fitting p-orbital peaks was selected as nearly 0.5. We followed the fitting models described in www.xpsfitting.com. The considerations of physical and chemical plausibility of the used models were done in agreement with the predictions of thermochemical calculations. We aimed to elucidate the structure and composition of the surface oxides, contributing to our understanding of the Hybrid steel's corrosion resistance and overall performance, and not to provide a comprehensive quantitative description of the surface structure.

Thermochemical modelling

A CalPhaD-based modelling procedure was addressed to estimate solid products and some critical dissolved ions by interfacial reactions to understand the native surface oxide compounds and corrosion products due to anodic polarization. The FactSage 8.2 thermochemical software was used with two distinct databases[36,37], namely the FThelg solution database, which contains infinite dilution properties for over 1400 aqueous solutes, and the FactPS database, which includes thousands of thermodynamic data for stoichiometric phases in solid, liquid, gas and ionic states.

The principle behind the modelling is based on the local equilibrium, assuming that only thermodynamic principles are valid at the interface between the steel and aqueous solution. The chemical and electrochemical reaction products of *Hybrid* steel with the corrosive environments have been simulated. The (Fe-Ni-Cr-Al)-H_2O-H_2SO_4-O_2 system has been used to calculate the corrosion products (aqueous and solid) and their molalities in acidic sulfuric acid (pH 0.3–3). The (Fe-Ni-Cr-Al)-H_2O-NaCl-O_2 system was used to compute the surface oxides and corrosion products in near-neutral aqueous chloride solutions. We used steel molalities (concentration) between 1 and 10 M to provoke the metal's oxidation process, which is the Eh change in the near-surface region (high steel content) at a given initial pH and temperature[36,37]. Herein, the experimentally-obtained electrochemical potentiodynamic polarization curves served as valuable input data, and several reiterated cross-checks were made to refine the computational model.

Kinetical constraints dominate the polarization process. However, a reaction is only possible when the thermodynamic conditions exist. We have overcome the kinetical limitations by assuming various dissolving metal molalities (1–1000's of mole), the latter being the Hybrid steel. Only those computational results matching the measured polarization curves were reported herein. Hence, the CalPhaD computational analyses provided information about the interfacial pH change associated with metal oxidation. The effect of the oxygen pressure (fugacity) was used to calculate the overpotential in the aqueous solution, simulating anodic polarization. The general approach was validated previously in successfully creating aqueous phase diagrams in FactSage, thanks to well-defined relationships among the oxygen potential, log $p(O_2)$, the hydrogen potential, log $p(H_2)$, Eh, and pH[38]. It should be emphasized that FactSage modelling is not just a calculation based on theoretical background. Instead, it accesses experimentally documented data and calculates a model system's aqueous and solid compounds in aqueous solutions. The computations are based on thermodynamical equilibria and show stable conditions. However, we have altered the model to get an idea about the kinetics associated with the electrochemical polarization and to assess the surface oxides/oxyhydroxides of the *Hybrid* steel.

Our research has culminated in a significant advancement in materials science, showcasing the ability to bestow steel with passive behaviour through an efficient alloying recipe with a chromium concentration as low as five weight percent. The electrochemical potentiodynamic polarization measurements have confirmed that *Hybrid* steel exhibits all the characteristic features that make steel stainless, including passivity, breakdown, and pitting, comparable to standard low-alloyed stainless steel. The exceptional stainless nature of Hybrid steel is attributed to the formation of a dynamically protective nanometre-sized passive film consisting of iron, chromium, nickel, and aluminium oxides, as revealed by synchrotron hard X-ray photoelectron spectroscopy analysis. The thermodynamic calculations have provided valuable insights into the surface oxide composition, predominantly comprising $Fe_2O_3 \cdot FeCr_2O_4 \cdot NiO \cdot Al_2O_3$, which exhibits structural changes, varying fractions, and dynamic existence during electrochemical polarization.

Notably, it has been elucidated that the presence of aluminium and nickel plays a pivotal role in supporting chromium in forming a spontaneously passive and protective surface. This intricate synergy yields exceptional corrosion resistance in acidic and chloride-containing aqueous environments. Remarkably, the surface oxide of Hybrid steel exhibits remarkable stability, even after transpassing the Cr(III)-to-Cr(VI) redox potential. This property sets it apart from conventional stainless steels.

Our findings also shed light on the adverse effects of chromium on grade 304 and 420 stainless steel when Cr(VI) species are released, leading to the destruction of the passive film due to extensive interfacial pH reduction. In contrast, Hybrid steel stands out as it can readily repassivate, thanks to the presence and enrichment of aluminium and nickel oxides, which offer superior anodic passivation. This study showcases the power of delicate alloying and microstructure engineering in designing sustainable stainless steel with exceptional high-strength properties without relying on the well-known Cr threshold concentration of 10.5 percent. The insights gained from our research hold great promise for developing advanced stainless steel materials with remarkable corrosion resistance and enhanced mechanical properties, opening new avenues for engineering applications in harsh environments.

With this research, we contribute to the ever-evolving field of materials science and provide a stepping stone for future innovations in sustainable and high-performance alloy design. Our work highlights the importance of understanding the intricate

interplay between alloying elements and surface oxide formation, offering new perspectives for creating next-generation stainless steels with broader applications in various industries.

DATA AVAILABILITY

All data needed to evaluate the conclusions in the paper are present in the article, and further data is provided in the Supplementary Materials. Additional data related to this paper or the raw data may be obtained from the authors upon a reasonable request.

CODE AVAILABILITY

Not applicable.

Received: 8 January 2023; Accepted: 20 August 2023;
Published online: 28 August 2023

REFERENCES

1. Ryan, M. P., Williams, D. E., Chater, R. J., Hutton, B. M. & McPhail, D. S. Why stainless steel corrodes. *Nature* **415**, 770–774 (2002).
2. Qiu, J. H. Passivity and its breakdown on stainless steels and alloys. *Surf. Interface Anal.* **33**, 830–833 (2002).
3. Marcus P., Maurice V. The Structure of Passive Films on Metals and Alloys. In: Ives M. B., Luo J. L., Rodda J. R., editors. Passivity of Metals and Semiconductors; 1999; Jasper Park Lodge, Canada: The Electrochemical Society; 1999. p. 30–64.
4. Yue, X. et al. Passivation characteristics of ultra-thin 316L foil in NaCl solutions. *J. Mater. Sci. Technol.* **127**, 192–205 (2022).
5. Långberg, M. et al. Redefining passivity breakdown of super duplex stainless steel by electrochemical operando synchrotron near surface X-ray analyses. *npj Mater. Degrad.* **3**, 22 (2019).
6. Tranchida, G., Clesi, M., Di Franco, F., Di Quarto, F. & Santamaria, M. Electronic properties and corrosion resistance of passive films on austenitic and duplex stainless steels. *Electrochim. Acta.* **273**, 412–423 (2018).
7. Långberg, M. et al. Characterization of Native Oxide and Passive Film on Austenite/Ferrite Phases of Duplex Stainless Steel Using Synchrotron HAXPEEM. *J. Electrochem. Soc.* **166**, C3336–C3340 (2019).
8. Örnek, C., Leygraf, C. & Pan, J. Passive film characterisation of duplex stainless steel using scanning Kelvin probe force microscopy in combination with electrochemical measurements. *npj Mater. Degrad.* **3**, 8 (2019).
9. Långberg, M. et al. Lateral variation of the native passive film on super duplex stainless steel resolved by synchrotron hard X-ray photoelectron emission microscopy. *Corros. Sci.* **174**, 108841 (2020).
10. Maurice V., Marcus P. Structure, Passivation and Localized Corrosion of Metal Surfaces. In: Pyun S.-I., Lee J.-W. (eds). *Progress in Corrosion Science and Engineering I: Progress in Corrosion Science and Engineering I*. Springer New York: New York, NY, 2010, pp 1–58.
11. Olsson, C. O. A. & Landolt, D. Passive films on stainless steels—chemistry, structure and growth. *Electrochim. Acta.* **48**, 1093–1104 (2003).
12. Olsson, C.-O. A. The influence of nitrogen and molybdenum on passive films formed on the austenoferritic stainless steel 2205 studied by AES and XPS. *Corros. Sci.* **37**, 467–479 (1995).
13. Örnek C., et al. Exploring Hydride Formation in Stainless Steel Revisits Theory of Hydrogen Embrittlement. In: University C, editor.: arXiv; 2022. p. 31.
14. Mazurkiewicz, B. Anodic passivity of iron in sulphuric acid. *Electrochim. Acta.* **38**, 495–502 (1993).
15. Heine B. Untersuchungen an Eisen und Chrom sowie deren Legierungen zur Bildung und Zusammensetzung der Passivschichten auf diesen Werkstoffen. PhD thesis, University of Stuttgart, Stuttgart, 1988.
16. Cottis B., et al. Shreir's Corrosion - Volume 2. In: Cottis B., et al., editors. Fourth Edition ed. Manchester: Elsevier B.V., 2010.
17. Williams, D. E., Newman, R. C., Song, Q. & Kelly, R. G. Passivity breakdown and pitting corrosion of binary alloys. *Nature* **350**, 216–219 (1991).
18. Andersson J-E, Lindberg F., Ooi S. Hybrid Steel and Its Potential for Bearing Applications. *12th International Symposium on Rolling Bearing Steels*: ASTM International; 2020. pp. 436–454.
19. Yen, H. W., Chen, C. Y., Wang, T. Y., Huang, C. Y. & Yang, J. R. Orientation relationship transition of nanometre sized interphase precipitated TiC carbides in Ti bearing steel. *Mater. Sci. Technol.* **26**, 421–430 (2010).
20. Huang, C.-Y. & Yen, H.-W. HRTEM investigations on nano precipitates in Custom 475 maraging stainless steel. *Mater. Charact.* **178**, 111216 (2021).
21. Örnek, C., Davut, K., Kocabaş, M., Bayatlı, A. & Ürgen, M. Understanding Corrosion Morphology of Duplex Stainless Steel Wire in Chloride Electrolyte. *Corros. Mater. Degrad.* **2**, 397–411 (2021).
22. Örnek, C., Zhong, X. & Engelberg, D. L. Low-Temperature Environmentally Assisted Cracking of Grade 2205 Duplex Stainless Steel Beneath a MgCl2:FeCl3 Salt Droplet. *Corrosion* **72**, 384–399 (2016).
23. Tougaard, S. Practical guide to the use of backgrounds in quantitative XPS. *J. Vac. Sci. Technol. A* **39**, 011201 (2021).
24. Choudhary, S., Zhang, S., Thomas, S. & Birbilis, N. A Closer Look at the Passivity and Transpassive Dissolution of Chromium Using Atomic Spectro-electrochemistry. *ECS Adv.* **1**, 011501 (2022).
25. Potgieter, J. H. et al. Influence of nickel additions on the corrosion behaviour of low nitrogen 22% Cr series duplex stainless steels. *Corros. Sci.* **50**, 2572–2579 (2008).
26. Oldfield, D. J. W. Nickel effect: Lower rate of corrosion in stainless. *Emerald Group Publ. Ltd.* **37**, 9–11 (1990).
27. Eroğlu B. Corrosion and Corrosion Protection Properties of Binary Fe-Al Alloys Intermetallics. MSc thesis, Istanbul Technical University, Istanbul, 2021.
28. Anantha, K. H. et al. In Situ AFM Study of Localized Corrosion Processes of Tempered AISI 420 Martensitic Stainless Steel: Effect of Secondary Hardening. *J. Electrochem. Soc.* **164**, C810–C818 (2017).
29. Anantha, K. H. et al. Correlative Microstructure Analysis and In Situ Corrosion Study of AISI 420 Martensitic Stainless Steel for Plastic Molding Applications. *J. Electrochem. Soc.* **164**, C85–C93 (2017).
30. Ong S. P. First Principles Design and Investigation of Lithium-Ion Battery Cathodes and Electrolytes. Doctor of Philosophy thesis, Massachusetts Institute of Technology, Massachusetts, 2011.
31. Cao, P., Wells, D. & Short, M. P. Anisotropic ion diffusion in α-Cr2O3: an atomistic simulation study. *Phys. Chem. Chem. Phys.* **19**, 13658–13663 (2017).
32. Lorbeer, P. & Lorenz, W. J. A critical consideration of the flade potential. *Corros. Sci.* **21**, 79–86 (1981).
33. Schlueter, C. et al. The new dedicated HAXPES beamline P22 at PETRAIII. *AIP Conf. Proc.* **2054**, 040010 (2019).
34. Biesinger M. C. Advanced Studies of Transition Metal X-ray Photoelectron Spectra. University of South Australia, 2012.
35. Watts J. F., Wolstenholme J. *An introduction to surface analysis by XPS and AES*. John Wiley & Sons, 2019.
36. Bale, C. W. et al. FactSage thermochemical software and databases, 2010–2016. *Calphad* **54**, 35–53 (2016).
37. Jung, I.-H. & Van Ende, M.-A. Computational Thermodynamic Calculations: FactSage from CALPHAD Thermodynamic Database to Virtual Process Simulation. *Metall. Mater. Trans. B* **51**, 1851–1874 (2020).
38. Pelton, A. D., Eriksson, G., Hack, K. & Bale, C. W. Thermodynamic calculation of aqueous phase diagrams. *Monatshefte f.ür. Chem. - Chem. Monthly* **149**, 395–409 (2018).

ACKNOWLEDGEMENTS

This work was supported by TÜBITAK (The Scientific and Technological Research Council of Türkiye) under contract number 118C227 within the program 2232: International Fellowship for Outstanding Researchers. In addition, we acknowledge DESY (Hamburg, Germany), a member of the Helmholtz Association HGF, to provide experimental facilities. The synchrotron measurement was carried out at beamline P22 at PETRA III. Furthermore, HWY and CEC appreciate the financial support from the National Science and Technology Council (NSTC) in Taiwan (NSTC 109-2628-E-002-009-MY3).

AUTHOR CONTRIBUTIONS

C.Ö.: Conceptualization, Methodology, Software, Validation, Formal analysis, Investigation, Resources, Data curation, Writing – original draft, Writing – review & editing, Visualization, Supervision, Project administration, Funding acquisition. B.P.: Software, Validation, Formal analysis, Investigation, Data curation, Writing – review & editing, Visualization. A.G.: Software, Formal analysis, Investigation, Resources, Data curation, Writing – review & editing. K.K.: Software, Formal analysis, Writing – review & editing. N.M.: Software, Validation, Formal analysis, Investigation, Data curation. B.D.: Software, Formal analysis, Investigation, Resources, Data curation, Writing – original draft, Writing – review & editing. M.Ü.: Conceptualization, Methodology, Formal analysis, Resources, Writing – review & editing. B.A.: Software, Formal analysis, Investigation, Writing – review & editing. C.-E.C.: Software, Validation, Formal analysis, Investigation, Data curation. H.-W.Y.: Software, Validation, Formal analysis, Investigation, Data curation, Writing – review & editing. S.O.: Resources, Material provision, Writing – review & editing, Project administration, Funding acquisition.

COMPETING INTERESTS

The authors declare no competing interests.

ADDITIONAL INFORMATION

Supplementary information The online version contains supplementary material available at https://doi.org/10.1038/s41529-023-00392-z.

Correspondence and requests for materials should be addressed to Cem. Örnek.

Reprints and permission information is available at http://www.nature.com/reprints

Publisher's note Springer Nature remains neutral with regard to jurisdictional claims in published maps and institutional affiliations.